Check for updates

Nanostructured MnOx/g-C3N4 for photodegradation of sulfamethoxazole under visible light irradiation†

Oanh T. K. Nguyen, [ID] [a] Vinh Huu Nguyen, [ID] [a] Nong Xuan Linh,[a] Minh Que Doan,[a] Lan-Anh T. Hoang,[b] Taeyoon Lee*[b] and Trinh Duy Nguyen [ID] *[a]

The effectiveness of g-C3N4 as photocatalyst is hindered by the rapid recombination of photo-generated electron/hole pairs. To improve its photocatalytic performance, the incorporation of g-C3N4 with co-catalysts can promote charge separation efficiency and enhance redox capabilities. In our study, a two-step approach involving calcination and solvothermal method was utilized to fabricate a proficient MnOx/g-C3N4 heterojunction photocatalyst with high photocatalytic activity. MnOx is effective at capturing holes to impede the recombination of electron/hole pairs. The MnOx/g-C3N4 composite shows a notable improvement in photocatalytic degradation of SMX, obtaining an 85% degradation rate, surpassing that of pure g-C3N4. Furthermore, the MnOx/g-C3N4 composite exhibits remarkable and enduring catalytic degradation capabilities for sulfamethoxazole (SMX), even after four consecutive reuse cycles. The intermediates produced in the MnOx/g-C3N4 system are found to be less hazardous to common aquatic creatures such as fish, daphnids, and green algae when compared to SMX. With its high tolerance, exceptional degradation ability, and minimal ecological risk, the MnOx/g-C3N4 composite emerges as a promising candidate for eliminating antibiotics from wastewater resources.

1. Introduction

In recent decades, notable advancements have been achieved in clinical research, pharmaceuticals, and personal care products. However, despite their extensive application, these substances can pose a threat to natural aquatic ecosystems and urban wastewater effluents even at low concentrations.[1] Sulfamethoxazole (SMX), a widely utilized bacteriostatic sulfonamide, is frequently prescribed for conditions like urinary tract infections, toxoplasmosis, and sinusitis.[2] Because of its broad application, chemical stability, and poor biodegradability, SMX has been found in both freshwater bodies and wastewater systems.[3] As a refractory organic molecule, SMX proves challenging to eliminate through conventional treatment methods.[4] Previous research has confirmed the presence of SMX in wastewater, surface and groundwaters.[5,6] The concentration of SMX in these water matrices ranges from nanograms to micrograms per liter, with notably higher levels detected in hospital effluents.[6] Consequently, the development of

sustainable and innovative strategies is imperative to mitigate the accumulation of these emerging contaminants in natural water reservoirs.

g-C3N4 has sparked widespread interest for its robust photocatalytic activity and efficient light absorption characteristics. Its 2D layered nanostructure exhibits exceptional chemical, environmental, and thermal resilience, thanks to the robust covalent bonds between nitrogen and carbon atoms. With a band gap energy of 2.7 eV, g-C3N4 may efficiently use visible light for a variety of applications. Its conduction band energy (E_{CB}) and valence band energy (E_{VB}) make it well-suited for water-based oxidation and reduction processes.[7–9] Besides, g-C3N4 has a graphitic arrangement of layers linked by tertiary amines, resulting in a distinctive delocalized conjugated structure[10] and low electronic conductivity.[11,12] Furthermore, one key characteristic of g-C3N4 is its straightforward production process, which involves cost-effective and easily obtainable raw materials using a direct synthetic method. These features have resulted in its extensive application as a visible light-driven photocatalyst, with uses spanning organic compound degradation, water splitting, N2 fixation, and CO2 reduction.[13,14] Nevertheless, pure g-C3N4 exhibits several drawbacks, such as a limited range of responsiveness to visible light and a low efficiency in separating electron–hole pairs. These conditions greatly diminish its photocatalytic effectiveness.[15] Researchers have devised multiple methods to enhance the light absorption and electron–hole pair transfer capabilities of g-C3N4 and

[a]*Institute of Applied Technology and Sustainable Development, Nguyen Tat Thanh University, Ho Chi Minh City, Vietnam. E-mail: ndtrinh@ntt.edu.vn*

[b]*Department of Environmental Engineering, College of Environmental and Marine, Pukyong National University, 45 Yongso-ro, Nam-gu, Busan 48513, Republic of Korea. E-mail: badger74w@pknu.ac.kr*

† Electronic supplementary information (ESI) available. See DOI: https://doi.org/10.1039/d4ra05996d

improve photocatalytic performance. These strategies involve structure modification, defect engineering and composite modification.[13]

Recently, combination of g-C_3N_4 with nanostructured metal or metal oxides possessing a low band gap allows for the establishment of heterostructure nanohybrids, that exhibit outstanding photocatalytic activity under visible light irradiation. Within the N sites of g-C_3N_4, the electron-rich sp^2 N forms strong interactions with metal cations.[16,17] This adjustable strategy enables the change of parameters to achieved targeted band gap engineering.[18,19] The widespread use of g-C_3N_4 and surface-functionalized g-C_3N_4 nanostructured composite could prove useful in removal of organic pollutants in the water media. Among this strategy, combining g-C_3N_4 with other semiconductors to establish heterostructures with well-aligned band structures has been considered as an effective approach to prevent the recombination of charge carriers generated by photogenerated processes. The decoration of metal oxides on g-C_3N_4 has been extensively researched and applied in various fields, such as water splitting,[20] CO_2 reduction,[21,22] and the degradation of organic pollutants.[23–25] Some metal oxides, such as RuO_x, CoO_x, and MnO_x, exhibit efficacy in capturing holes to increase the separation efficiency of photogenerated electron–hole pairs.[26,27] For instance, Shuaiqi Zhao *et al.* reported that using MnO_x/g-C_3N_4 nanocomposites mediated sulfite activation for methyl orange (MO) decomposition. The photocatalytic reaction was performed with MO concentration (20 mg L^{-1}), catalyst dose (0.4 g L^{-1}), NaHSO$_3$ concentration (0.52 g L^{-1}), and at pH 5.2. The degradation rate of MO can reach as high as 94% within 20 min.[28]

Thus, this study aims to offer a straightforward procedure for synthesizing MnO_x/g-C_3N_4 nanocomposite materials catalyzed for the photodegradation of SMX antibiotics. Various MnO_x/g-C_3N_4 catalysts were produced and studied for varying Mn concentrations. Under LED light exposure, the catalytic efficacy of MnO_x/g-C_3N_4 in the breakdown of antimicrobial contaminants was examined. Through quenching tests, the underlying mechanism of SMX degradation and MnO_x/g-C_3N_4 activation was explored. The findings confirmed that under LED light exposure, the presence of MnO_x species facilitated the separation of photogenerated carriers and enhanced the generation of active radicals with the MnO_x/g-C_3N_4 composite.

2. Experimental

2.1. Materials and reagents

Thiourea, manganese chloride tetrahydrate ($MnCl_2 \cdot 4H_2O$), sodium oxalate ($Na_2C_2O_4$), potassium dichromate ($K_2Cr_2O_7$), and *N,N*-dimethylformamide (DMF) were all provided from Xilong Chemical Ltd. Sulfamethoxazole (SMX), *p*-benzoquinone (BQ), and *tert*-butyl alcohol (TBA) were acquired in a pure grade from Sigma Aldrich and used without additional treatment. Deionized water was used for all the trials.

2.2. Synthesis of MnO_x/g-C_3N_4 composites

The g-C_3N_4 was obtained by a four-hour calcination process of thiourea within a sealed crucible at 550 °C.[29] Subsequently, the g-C_3N_4 component modified with manganese was prepared using a solvothermal method (Fig. S1†). Initially, the g-C_3N_4 (0.2 g) was dispersed in a DMF solvent (60 mL) through sonication for 1 h. Afterwards, an appropriate amount of $MnCl_2 \cdot 4H_2O$ (6.73, 20.19, and 33.66 mg), corresponding to 1, 3, and 5 weight% of Mn was introduced into the solution mentioned above and continuously sonicated for 1 h at room temperature. The purpose of this process was to facilitate the insertion of Mn atoms into the suitable interstitial sites within the g-C_3N_4 crystal structure. The suspension was then transferred to a Teflon-line autoclave (100 mL) and underwent a 16 hour solvothermal process at 200 °C. Upon cooling the suspension to room temperature, the solid was collected using centrifugation, along with three washes utilizing DMF and ethanol to eliminate any residual impurities. The left-over substance was subjected to overnight drying at 85 °C to obtain MnO_x/g-C_3N_4. For a convenient, g-C_3N_4 photocatalyst modified with 0, 1, 3, and 5 weight% of Mn were donated as CN, 1MnCN, 3MnCN, and 5MnCN, respectively.

2.3. Characterizations

X-ray diffraction (XRD) patterns of MnO_x/g-C_3N_4 nanocomposites were analyzed by a D8 Advance diffractometer (Brucker, Germany). The Fourier Transformed Infrared (FTIR) spectra of the as-synthesized materials were obtained using a JASCO FT/IR-4X spectrometer from America. SEM pictures of the produced samples were acquired using a JSM-IT800 scanning electron microscope. The Brunauer–Emmett–Teller (BET) surface area was determined using a TriStar 3000 V6.07, an instrument manufactured by Micromeritics Instrument Corporation in the United States. UV-visible diffuse reflectance spectra (UV-vis DRS) were measured using a Shimadzu UV-2450 UV-Vis spectrophotometer. The photosensitive characteristics of the MnO_x/g-C_3N_4 samples were determined through UV-vis absorption spectra obtained from a UV-vis spectrophotometer (Model UV-2450, Shimadzu). The AXIS SUPRA spectrometer was utilized for X-ray photoelectron spectroscopy (XPS) measurements. A Cary Eclipse Fluorescence Spectrophotometer (Varian, Australia) was used to conduct photoluminescence (PL) spectra. The excitation wavelength was set at 380 nm and the temperature at 298 K.

2.4. Electrochemical measurements

Mott–Schottky (MS) plots, Nyquist plot analyses and transient photocurrent curves were performed on a single-channel electrochemical workstation (AUTOLAB-PGSTAT204, Metrohm), using a standard three-electrode system. The system comprises a Pt wire counter electrode, an Ag/AgCl reference electrode and catalyst/FTO working electrode. The fabrication process of catalyst/FTO working electrode involved dispersing photocatalyst (10 mg) in a solution comprising ethanol (1 mL) and Nafion solution (20 μL) to achieve a uniform suspension. Then, applying the suspension to the surface of the FTO substrate with about 5×15 mm^2 area using a spray deposition method. The catalyst/FTO was dried in a vacuum oven at 60 °C for 12 h. An electrolyte of 0.5 M Na_2SO_4 solution was utilized. Besides, the photocurrent method was performed in solution containing Na_2SO_4 0.5 M and Na_2SO_3 0.5 M.

2.5. Photocatalytic tests

The MnO_x/g-C_3N_4 materials were evaluated for their photocatalytic activity using the sulfamethoxazole (SMX) antibiotic as a degradation agent. Initially, 10 mg of MnO_x/g-C_3N_4 photocatalyst was used and evenly distributed in 100 mL of SMX solution with a concentration of 15 ppm (0.059 mmol dm^{-3}). The dispersion process was facilitated by ultrasound vibration for 3 minutes. The solution was agitated for 60 minutes in the absence of light to achieve an equilibrium state of adsorption–desorption. To assess equilibrium, a 3 mL portion of the solution was extracted after 60 minutes of vigorous stirring in the absence of light, to determine the residual concentration of SMX. Afterward, the solution was agitated under the irradiation of a white light LED lamp (40 W) as a visible light source. After every 60 minutes of exposure, a 3 mL sample of the solution was taken and passed through a filter to separate the photocatalyst. The UV-vis absorption spectra were measured at a wavelength of 267 nm. Alternatively, the samples were analyzed using high-performance liquid chromatography (HPLC) with a C18 reversed-phase column (4.6 mm × 250 mm) on a Sykam S600 system. The toxicity of SMX and its intermediates during photocatalysis was verified by the QSAR method *via* the ECOSAR program.[30]

To identify the active species generated during photocatalytic reaction, $Na_2C_2O_4$ (2 mM), BQ (2 mM), TBA (2 mM), and $K_2Cr_2O_7$ (2 mM) were used to as a photogenerated hole (h$^+$), superoxide radical ($^•O_2^-$), hydroxyl radical ($^•OH$), and electron (e$^-$) scavengers, respectively, with all similar other conditions.

3. Results and discussion

3.1. XRD analysis

The crystal phase of the CN and *x*MnCN samples show two distinct diffraction peaks at 13.06° and 27.56°, comparable to those seen in g-C_3N_4 without impurities (Fig. 1A). The 2θ at 27.56° corresponds to the (002) crystal plane, indicating the interlayer stacking in the aromatic system. The 2θ at 13.06° aligns with the (100) plane, indicating the in-plane structural arrangement of tri-*s*-triazine units.[31,32] The absence of MnO_x diffraction peaks indicates minimal loading and uniform distribution.[33] When the MnO_x content was increased to 5 wt%, weak diffraction peaks at 12.1°, 24.1°, and 36.6° emerged, corresponding to the (001), (002), and (100) facets of MnO_x, respectively,[34] indicating the production of MnO_x. Besides, the position of a series of peaks align with the reference patterns from the Crystallography Open Database (COD), including MnO (COD-1010393) (Fig. S2†),[35] Mn_2O_3 (COD-1514103) (Fig. S3†),[36] and MnO_2 (COD-1514239) (Fig. S4†),[37] suggesting the presence of manganese oxide in the synthesized samples. Based on the XRD patterns, it can be inferred that MnO_x was introduced as a dopant onto g-C_3N_4.

3.2. FT-IR analysis

The FT-IR spectra of both pure CN and *x*MnCN samples exhibit striking similarities (Fig. 1B). The wavenumbers at 1639 and 1578 cm^{-1} relate to C=N group stretching vibrations, whereas those at 1463, 1413, 1319, and 1241 cm^{-1} relate to aromatic C–N stretching vibrations.[38] The wavenumber observed at 810 cm^{-1}
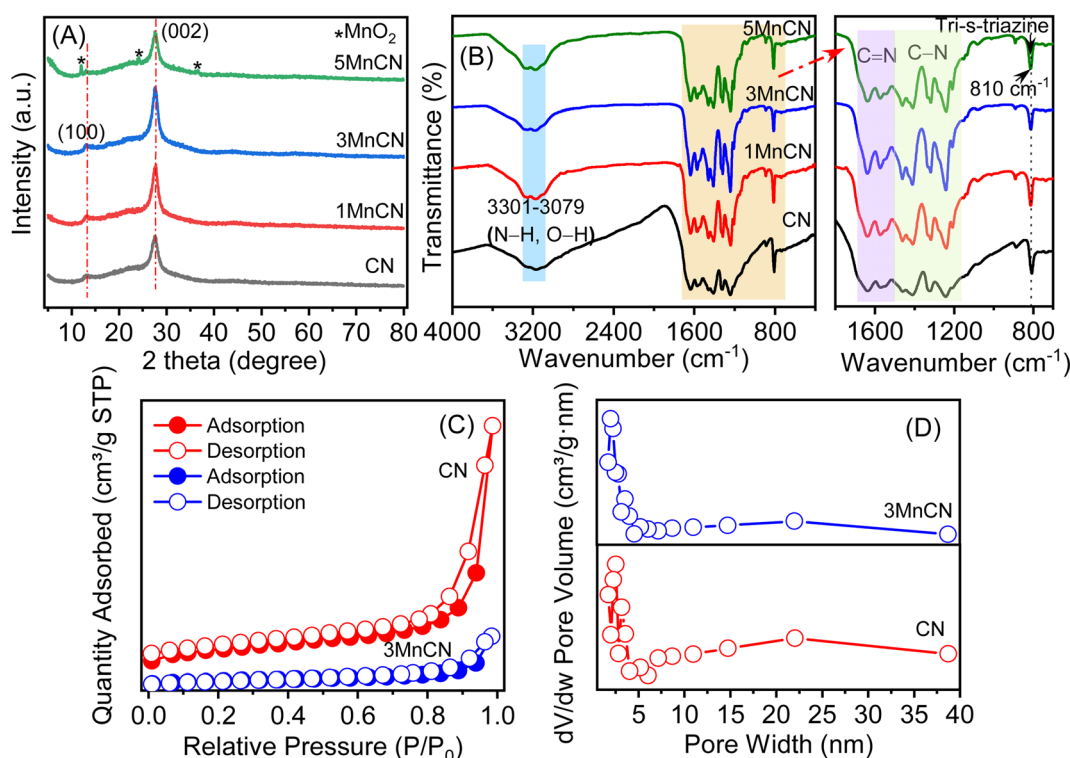

Fig. 1 (A) XRD pattern, (B) FT-IR spectra of CN, 1MnCN, 3MnCN, and 5MnCN; (C) N$_2$ adsorption–desorption isotherms, and (D) pore width of CN and 3MnCN.

relates to the breathing mode of tri-*s*-triazine units.[39] The wave numbers in the range of 3301–3079 cm^{-1} indicate stretching vibrations of N–H or O–H units.[40] These typical FT-IR peaks suggest that the general structure of CN remains unaltered following MnO$_x$ loading.

3.3. N$_2$ adsorption–desorption isotherms

Fig. 1C and D show N$_2$ adsorption–desorption isotherms that were utilized to evaluate the textual properties of the CN and 3MnCN, respectively. The hysteresis loops of CN and 3MnCN were classified as H3, indicating the presence of slit-shaped pores created by aggregated flake-like components.[41] The S_{BET} values for CN and the 3MnCN nanocomposite were 44 and 8 m^2 g^{-1}, respectively (Table S1†). Modifying CN with MnO$_x$ resulted in a considerable reduction in surface area, which may be insufficient to increase photocatalytic efficiency. Furthermore, the total pore volume and average pore width of the 3MnCN fluctuated erratically. As a result, there is no notable alteration in textual properties width after MnO$_x$ alteration of CN, demonstrating that surface-related parameters are not the key variables influencing photocatalytic efficiency.

3.4. Morphological observation

The morphology and structure of pure CN and *x*MnCN nanocomposites was examined *via* SEM (Fig. 2A–D) and TEM

(Fig. 2E and F) analysis. Fig. 2A shows that the as-prepared CN sample has a characteristic layered structure, with the surface made up of stacked nanosheets. After alteration, the morphologies of the *x*MnCN samples remained intact, as illustrated in Fig. 2B–D. However, the deposition of MnO$_x$ nanoparticles onto CN increases surface texture and roughness as a result of the MnO$_x$ particles. Depending on their size and distribution, these particles may form small bumps or clusters on the otherwise smooth surface of CN. This addition also enhances the material's porosity, leading to a rougher and more uneven appearance in SEM images compared to pure CN.[42–44] The pristine CN indicates a crumpled layered structure was observed by TEM images (Fig. 2E). As presented in Fig. 2F, there are no obvious change in 3MnCN sample, it exhibits layered structure without clear crumple and no nanoparticle turned up on the 3MnCN surface. Fig. 2G and G1 show the EDS mapping diagram for 3MnCN, which depicts the element distributions on the catalyst surfaces. The EDS-mapping images (Fig. 2G2–G5) display that N, O, C, and Mn elements are evenly distributed in 3MnCN, demonstrating that Mn is evenly distributed and completely covered the CN surface. Fig. S6† shows the characteristic peaks for C, N, O, and Mn. Although the Mn content in 3MnCN is low, the Mn peak is visible and requires further confirmation *via* XPS spectra, as seen below.
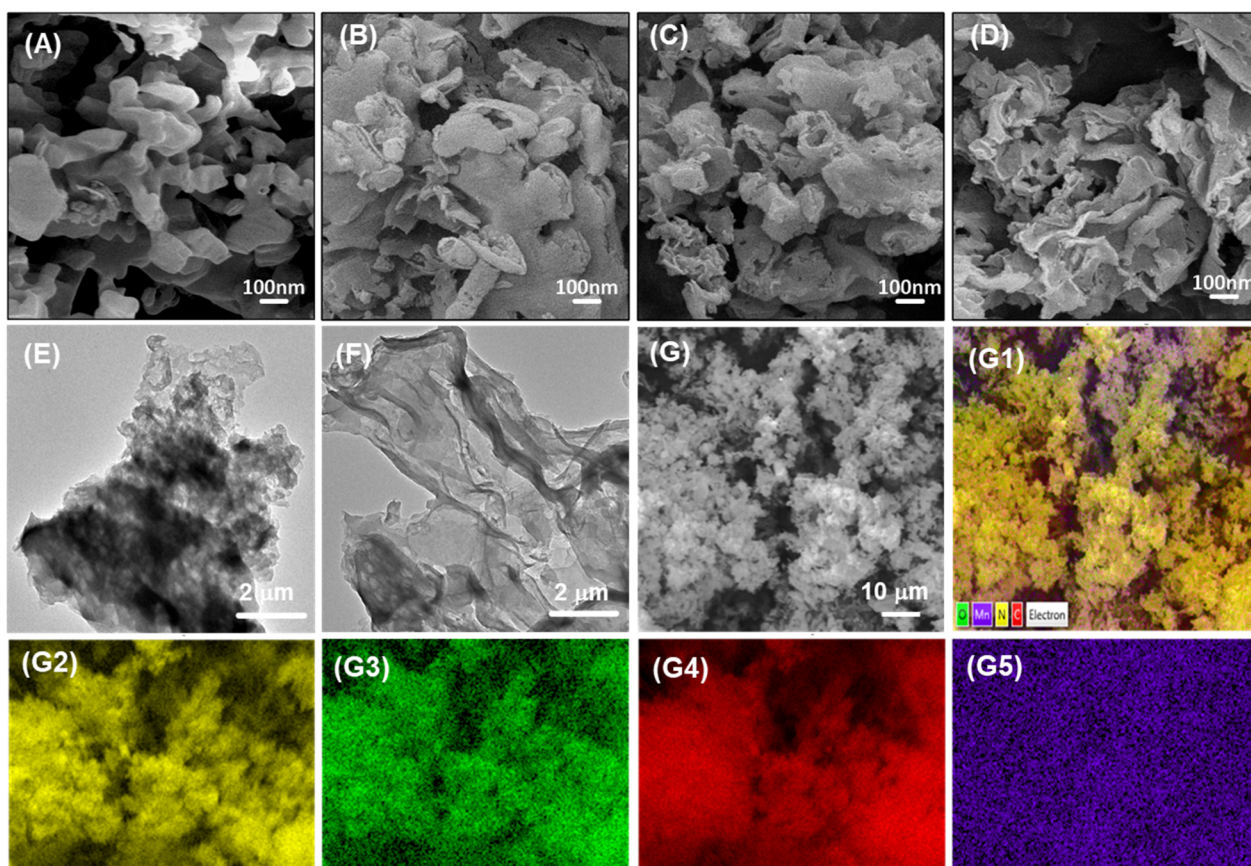

Fig. 2 SEM images of CN (A), 1MnCN (B), 3MnCN (C), and 5MnCN (D); TEM images of CN (E) and 3MnCN (F); EDS mapping analysis of 3MnCN (G). SEM image of the selected-area EDS (G1), and the elemental distribution images of N (G2), O (G3), C (G4), and Mn (G5).

3.5. Raman analysis

Raman spectroscopy is commonly employed to investigate the vibrational characteristics of carbon-based materials. Fig. S5† presents the Raman spectra for CN and 3MnCN samples across the 50–2500 cm^{-1} range. The Raman spectrum of the pure CN sample displayed peaks at 546, 673, 1314, and 1583 cm^{-1}. The peaks at 546 and 673 cm^{-1} are linked to the breathing modes of the *s*-triazine ring within the CN structure.[45] The extra peaks at 1314 and 1583 cm^{-1} are linked to structural defects or irregularities in the graphite framework and to the stretching modes of the C=C bond,[45] respectively. In the 3MnCN sample, peaks appear at 1325 and 1596 cm^{-1}, also corresponding to the C=C bond but slightly shifted to the right compared to pure CN.[46] Overall, Raman shifts may be influenced by the electromagnetic interactions between MnO$_x$ and the CN network.

3.6. XPS analysis

Fig. S7† depicts the XPS spectra of CN and 3MnCN for investigating the surface compositions and valence states. While C, N, and O were detected in both samples, Mn was exclusively found in the 3MnCN sample.

Fig. 3A depicts the high-resolution spectra of C 1s, which are separated into two different components. The binding energy (BEs) observed at 284.5 and 287.8 eV correspond to C atoms in the C–C and N=C–N groups of heptazine units.[47,48] Both CN and 3MnCN have identical C 1s XPS spectra, indicating that metal atoms did not establish coordination bonds with C atoms and were not doped onto CN *via* atoms.[49] The O 1s spectrum of CN shows BEs at 532.2 and 533.7 eV (Fig. 3B), which correspond to the O–H coordination of surface hydroxyl groups and (CN)$_n$–O, respectively.[50] However, the O 1s spectrum of 3MnCN exhibits the additional component at a BE of 530.5 eV, associates with Mn–O–Mn bonding, validating the synthesis of the 3MnCN composite.[51] The N 1s XPS spectra of CN and 3MnCN (Fig. 3C) exhibit BEs at 398.3, 399.6, 400.8, and 404.1 eV, which correspond to sp^2-bonding N in C–N=C, bridging N in N–(C)$_3$, amino N in terminal C–NH$_2$ groups, and π-excitation, respectively.[52–54]

The high-resolution Mn 2p spectrum of 3MnCN shows two prominent peaks: Mn 2p$_{3/2}$ and Mn 2p$_{1/2}$. The peaks at 640.52, 642.54, and 646.54 eV correspond to Mn^{2+}, Mn^{3+}, and Mn^{4+} of Mn 2p$_{3/2}$, whereas the peaks at 652.21, 654.06, and 657.19 eV correspond to Mn^{2+}, Mn^{3+}, and Mn^{4+} of Mn 2p$_{1/2}$, respectively.[55] Therefore, the existence of MnO$_x$ on g-C$_3$N$_4$ layers indicates a mixture of MnO, Mn$_3$O$_4$, and MnO$_2$. The distribution of Mn in different valence states was determined by evaluating the ratios of the peak areas in the XPS spectra (Table S2†). The percentage of Mn^{4+} is predominant, suggesting that Mn occurs in the high valence states of Mn^{4+}, Mn^{3+}, which can serve as active centers for photocatalytic activity.[56,57]
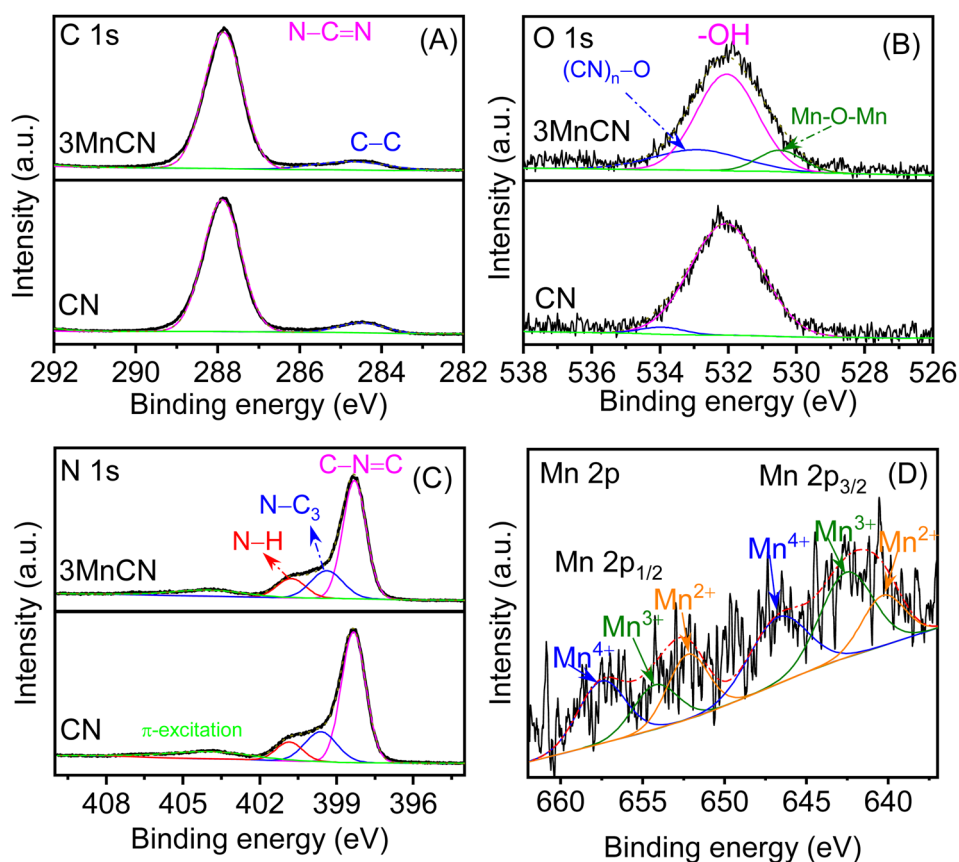

Fig. 3 XPS spectra of CN and 3MnCN. High resolution C 1s (A), O 1s (B), N 1s (C), and Mn 2p (D).

3.7. Photochemical characteristics and band gap calculation

The photochemical characteristics of CN and xMnCN were assessed using UV-DRS measurements. All samples displayed strong visible light absorption, with a pronounced absorption edge within the 400–800 nm wavelength region (Fig. 4A). This absorption phenomenon is attributable to the transition electron between the lone pair VB and the π* CB in g-C_3N_4.[58] The bandgap energy of the CN and xMnCN materials were estimated using the Kubelka–Munk method (Fig. S8 and Table S1†).[59,60] Fig. S8† shows that the presence of MnO_x slightly decreased bandgap energy of CN.

3.8. Photoluminescence spectra

The PL spectra of the CN and xMnCN samples were evaluated to explore the enhancement of photogenerated charge carrier dynamics within MnO_x/g-C_3N_4 heterojunction (Fig. 4B). In the PL spectrum of pure CN, a wide peak centered at 455 nm was observed, suggesting that the emission originated from the charge transition between the lowest unoccupied molecular orbital and the highest occupied molecular orbital of CN.[60] Besides, among all samples, 3MnCN exhibited the weakest PL intensity, indicating the significant reduced recombination rate of photogenerated electron holes.[61] This outcome provides the integration of MnO_x and g-C_3N_4 can promote the separation of electron–hole pair. However, the 5MnCN sample, characterized by excessive MnO_x loading, displayed an elevated PL intensity, indicating a faster recombination rate of photogenerated carriers.

3.9. Photoelectrochemical performance

The investigation of interfacial charge transfer in CN and 3MnCN samples was conducted using electrochemical impedance spectroscopy (EIS) Nyquist plots (Fig. 4C). The 3MnCN sample has a diminished arc radius in contrast to the CN sample, indicating a decrease in charge transfer resistance,[62,63] which is consistent with the PL spectra.

Fig. 4D depicts the transient photocurrent curves of CN and 3MnCN throughout irradiation intervals. The current intensity of both samples exhibited cyclic fluctuations corresponding to the on–off cycles of the light source, indicating their heightened photosensitivity. The 3MnCN photocatalyst showed a higher photocurrent intensity (0.51 μA cm^{-2}) compared to CN (0.25 μA cm^{-2}). This results provides additional confirmation of enhanced charge separation within MnO_x/g-C_3N_4 heterojountion.

The CB positions of the CN and 3MnCN were assessed by means of Mott–Schottky plots (Fig. 4E and S9†) to calculate the flat-band potential. The 3MnCN sample exhibits a lower negative E_{fb} (−0.49 eV $vs.$ NHE) than CN (−0.44 eV $vs.$ NHE). The CB edges of CN and 3MnCN are −0.74 eV and −0.80 eV, the VB edges of CN and 3MnCN are +1.96 eV and +1.99 eV, respectively. The comparison of the experimental data demonstrates the observed trend, and Fig. 4F provides a schematic representation of the band structure of 3MnCN systems. The electron transfer from MnO_x to CN is what causes the increase in the Fermi level of CN at greater MnO_x concentrations. Consequently, the locations of E_{CB} and E_{VB} shift upwards with the Fermi level. The
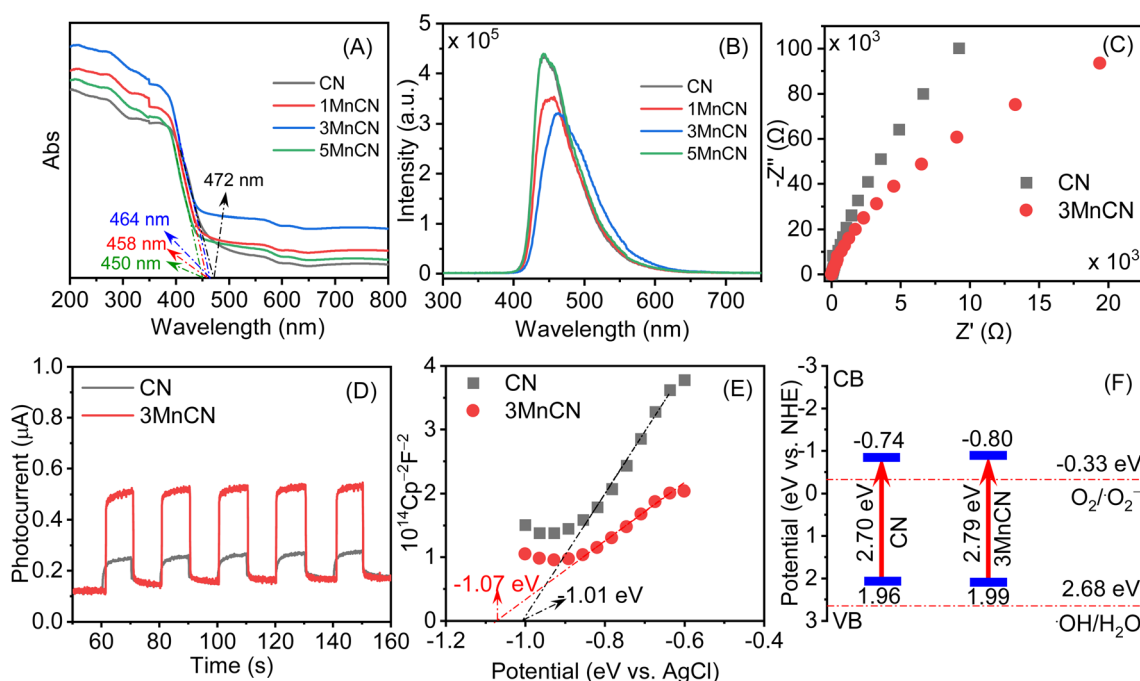

Fig. 4 UV-vis diffuse reflectance spectra (A) and PL spectra (B) of as prepared CN, 1MnCN, 3MnCN, and 5MnCN; the electrochemical impedance spectra (EIS) (C), transient photocurrent curves (D), Mott−Schottky plots (E), and band structures (F) of CN and 3MnCN.

upward movement of the band edge is essential in the photo-catalytic process. The increased elevation of E_{VB} facilitates the reaction between photo-generated holes and oxygen molecules, resulting in the production of superoxide ions. This enhances the oxidation capacity of holes in E_{VB}. Ultimately, the band edge undergoes an upward shift following the modification with MnO_x, which is accountable for the enhancement in photocatalytic efficiency.[64]

3.10. Photocatalytic activity

The photocatalytic activity of MnO_x modified CN in destroying SMX under LED light conditions was assessed (Fig. 5 and Table S3†). In the absence of light, minimal adsorption of SMX was noted for CN and x5MnCN samples. The results showed that concentration of SMX slightly increase after adsorption–desorption equilibrium compared to initial concentration (Fig. 5A). This outcome can be attributed to several factors. First, the adsorption of SMX molecules on the surface of catalysts may be weak or reversible. After initial adsorption, SMX molecules can desorb back into the solution, especially if the interaction between SMX and the catalyst surface is insufficiently strong. This could result in a minor increase in SMX concentration following equilibrium.[65] Additionally, changes in system conditions, such as temperature or pH during adsorption–desorption, can affect the equilibrium. For instance, shifts in equilibrium or a surface reaction between the SMX and the catalyst desorption may induce desorption, resulting in an apparent increase in SMX concentration post-equilibrium.[66] Furthermore, fluctuations in experimental conditions, such as stirring speed, temperature, or pH may influence adsorption dynamics. If these variables are not strictly controlled, minor desorption of SMX molecules could occur, contributing to the observed concentration after the equilibrium period.[67] However, a significant reduction trend in SMX removal was observed after turning on the LED lamp. Fig. 5A shows the comparative efficiency of SMX elimination among pure CN and x5MnCN catalysts. The degradation rate of SMX was estimated with an initial concentration of SMX of 15 mg L^{-1}. Bare CN demonstrates lower photocatalytic performance for SMX removal due to its elevated charge recombination rate, resulting in degradation rates of approximately 1%. In contrast, MnO_x/CN composites demonstrates substantially improved photocatalytic degradation efficiencies in SMX elimination. 1MnCN and 5MnCN achieved SMX degradation efficiencies of 75% and 52%, respectively, while 3MnCN demonstrates the highest degradation efficiency at roughly 85%.

Fig. 5B and Table S1† depict that the 3MnCN material exhibits a significantly higher rate constant (7.9×10^{-3} min^{-1}) compared to pure CN (0.02×10^{-3} min^{-1}), 1MnCN (6.1×10^{-3} min^{-1}), and 5MnCN (3.6×10^{-3} min^{-1}). The rate constant was estimated with an initial concentration of SMX of 15 mg L^{-1}. This outcome suggests that incorporation of MnO_x onto the CN surface enhances its photocatalytic efficacy. The chemical bonding interaction between MnO_x and CN facilitate
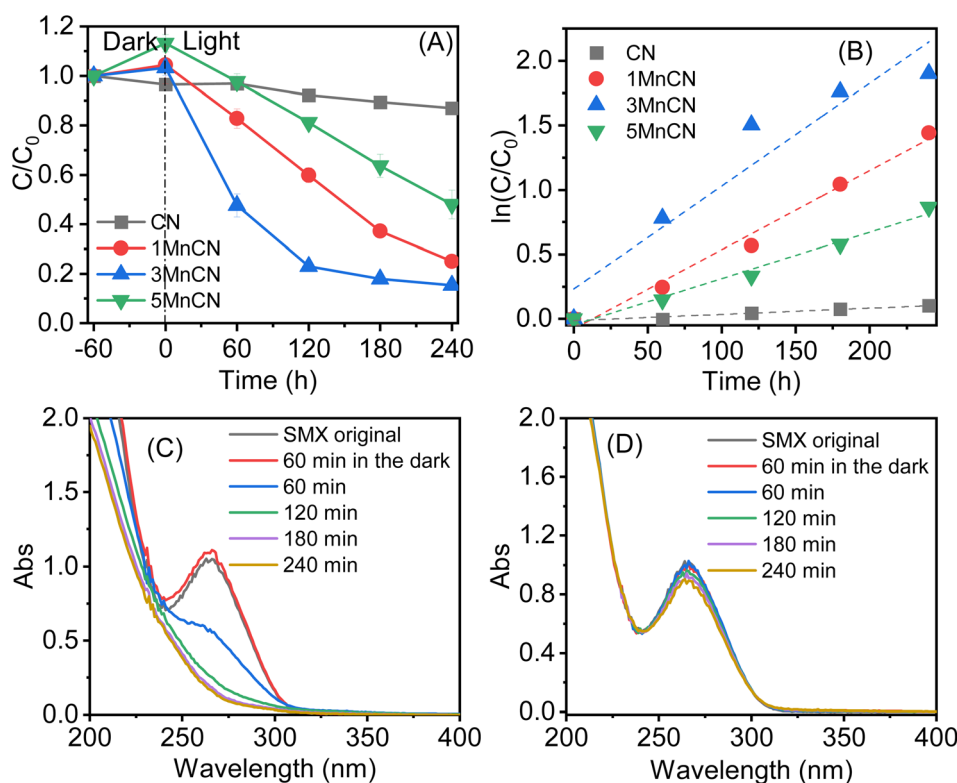

Fig. 5 Effect of different photocatalyst on (A) photodegradation of SMX, and first-order kinetics plots (B) for CN, 1MnCN, 3MnCN, and 5MnCN; UV-Vis spectra for photodegradation of SMX ($\lambda = 267$ nm) on 3MnCN (C) and CN (D). Conditions: [SMX]$_0$ = 15 mg L^{-1}, [CN]$_0$ (or [xMnCN]$_0$) = 200 mg L^{-1}, V = 100 mL, light source: 40 W white LED lamp. The source data is presented in Table S3.†

efficient transfer of photogenerated carriers, thereby minimizing the charge recombination, improving overall performance and ensuring stability in photocatalytic processes.[68] The degradation of SMX solution in the presence of 3MnCN and CN also presented *via* the UV-Vis adsorption spectra (Fig. 5C and D). Furthermore, Fig. S10† displays the HPLC results of SMX photodegradation catalyzed by the 3MnCN catalyst. After 240 minutes of photocatalytic reaction, no distinct peaks were evident, indicating that the near-complete degradation of the parent substances.

3.11. Effect of catalyst dosage and pH

The photocatalytic efficiency is significantly affected by the pH level since its influence on the characteristics of the catalyst like surface charge. In Fig. 6A, the degradation efficiency of SMX over 3MnCN photocatalyst was depicted in varying pH levels from 3 to 9. The result indicates that acidic pH levels result in better removal efficiency of SMX than basic pH levels. Interestingly, 3MnCN exhibits optimal performance at pH 5, achieving an 85% breakdown efficiency of SMX, with a corresponding rate constant of approximately 7.9×10^{-3} min^{-1} (Fig. 6B and Table S4†). SMX has a pK_a value of roughly 5.65,[69] indicating that its molecular state persists under acidic conditions, but SMX is negatively charged above pH 5.65. The zero-point charge (pH_{zpc}) for 3MnCN is determined as 3.7 (Fig. S11†), revealing that the surface of 3MnCN carries

a positive charge below this value, with an inversely proportional trend observed above this threshold. In acidic conditions, the complementary charges of SMX and the catalyst surface foster enhanced interaction, resulting in more effective photodegradation of SMX. At basic pH levels, however, the removal effectiveness diminishes due to both the catalyst surface and SMX bear similar surface charges. As a result, the pH of 5 was identified as optimal value for all following studies.

The amount of catalyst employed in the oxidation process has a major impact on the effectiveness of eliminating SMX antibiotics. Fig. 6C and Table S5† demonstrate the influence of various catalyst loadings, ranging from 0 to 300 mg L^{-1}, on the SMX elimination during photocatalytic degradation. In the absence of a catalyst, no degradation of SMX occurs under radiation, resulting in minimal SMX elimination. The presence of photocatalyst significantly improves SMX removal efficiency. Specifically, increasing 3MnCN catalyst doses from 100 mg L^{-1} to 300 mg L^{-1} improves removal efficiency from 56% to 73%. The corresponding kinetic outcomes are illustrated in Fig. 6D. The rate constants for the photodegradation of SMX usually increased as the catalyst dose increased, reaching a maximum of 200 mg L^{-1}. Nevertheless, when the quantity of catalyst was raised to 300 mg L^{-1}, the degradation rates of SMX decreased. Therefore, the optimum dosage of 3MnCN for maximal efficiency is determined to be 200 mg L^{-1}. This improvement is ascribed to the increased surface area of the catalyst, which
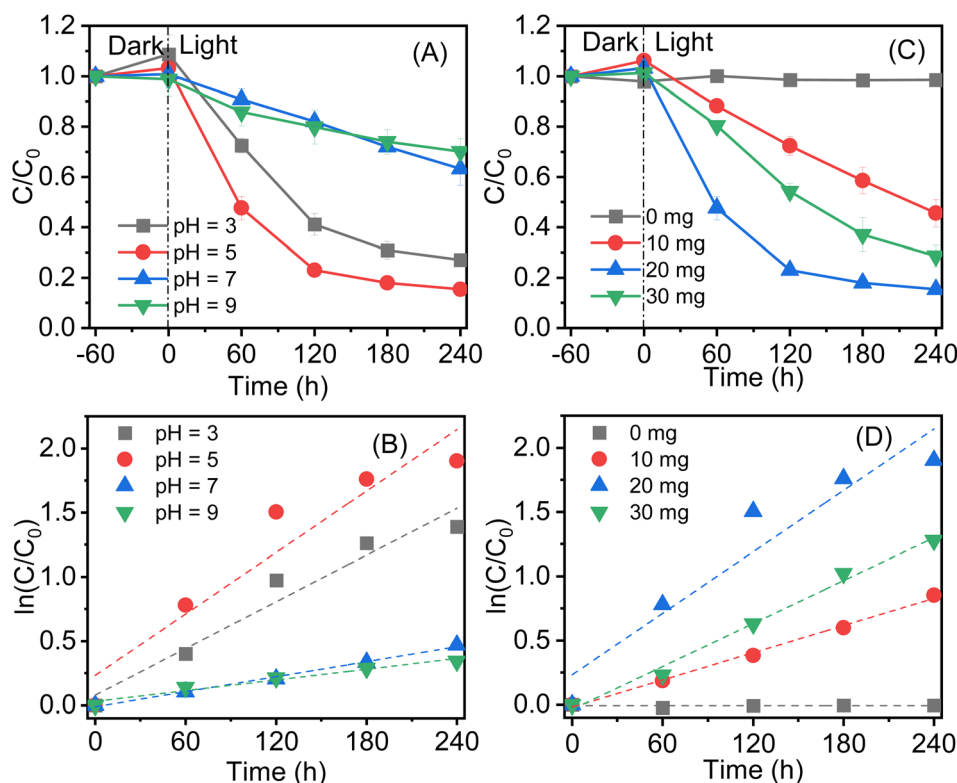

Fig. 6 Effect of initial pH on (A) SMX photodegradation, and first-order kinetics (B) plots; effect of various photocatalyst weight on (C) degradation of SMX and first-order kinetics (D) plots; conditions: $[SMX]_0 = 15$ mg L^{-1}, 3MnCN as a photocatalyst, V = 100 mL, light source: 40 W white LED lamp. The source data is presented in Tables S4 and S5.†

allows for the formation of more active radicals that degrade SMX.[70] However, an excessive catalyst dose can cause turbidity, dispersing incident light and inhibiting photon absorption by the catalyst, thereby limiting active radical production. Considering removal efficiency and production cost, a catalyst dosage of 200 mg L^{-1} was selected for subsequent studies.

3.12. Photocatalytic mechanism

To elucidate the reaction mechanism for SMX elimination over 3MnCN under optimal experimental conditions, the primary active species formed during photodecomposition were examined by analyzing reactive oxygen species (ROSs). Various scavengers, including $K_2Cr_2O_7$, $Na_2C_2O_4$, TBA, and BQ, were employed in active species quenching experiments to inhibit active e^-, h^+, $\cdot OH$, and $\cdot O_2^-$.[71] Fig. 7A depicts the roles of ROSs in the photocatalytic degradation of SMX over 3MnCN photocatalyst. The presence of $K_2Cr_2O_7$ and BQ resulted in a significant negative impact on the photodegradation rate of SMX compared to the control test, indicating that the photodegradation of SMX is predominantly driven by $\cdot O_2^-$ and e^- radicals.

The SMX degradation mechanism based on the experiment data for the 3MnCN/LED light system is depicted in Fig. 7B. When exposed to LED light, the electrons in VB position of CN undergo a transfer to the CB position, resulting in the generation of holes in the VB. Then, the photogenerated holes in VB would relocate to the surfaces of MnO_x, since MnO_x has the ability to efficiently collect photogenerated holes.[72] Subsequently, the photoexcited holes in the VB of CN and MnO_x might undergo a reaction with OH^- to produce $\cdot OH$, which in turn destroy SMX molecules. Furthermore, the highly stimulated electrons in the CB of monolayer CN suffer a reaction with O_2, resulting in the production of $\cdot O_2^-$ radicals. Similarly, the photoinduced holes in the VB of MnO_x actively contributes to the degradation of SMX.

3.13. SMX *photodegradation pathways and toxicity assessment*

The intermediate substances of SMX photodegradation were discovered by LC-MS. Fig. 8A depicts the SMX breakdown pathway, as determined by these LC-MS results (Fig. S12A–D†). Initially, the signal at $m/z = 253$ at 0 minutes of irradiation reflects SMX, which steadily diminishes in intensity with prolonged irradiation. During LED light exposure, the electrophilic addition of $\cdot O_2^-$ to C14 and C13 of the isoxazole ring results in the production of P1, a dihydroxylated SMX, a common mechanism in advanced oxidation processes of photocatalysis.[73] Then, $\cdot O_2^-$ attacks S7–N11 of SMX, producing P2 and 4-aminobenzenesulfonic acid. Although 4-aminobenzenesulfonic acid was not found, the production of P3, a result of 4-aminobenzenesulfonic *via* $\cdot O_2^-$ substitution, indicates its involvement in this route. The presence of P4 may stem from the cleavage of intermediate product P2 *via* SO_2 extrusion.[74] Furthermore, the presence of P3 and P5 could be attributed to SMX desulfonation products caused by the loss of SO_2 ions during $\cdot O_2^-$ oxidation.[75] This SO_2 desulfonation and rearrangement process entails three stages: breaking the arylsulfone bond (C–S), breaking the sulfonamide bond (S–N), and SO_2 extrusion.[74] Previous studies have also documented desulfonated intermediate products.[74,76,77] The degradation of these intermediate progresses, yielding smaller molecules such as P6, P7, and P8, ultimately resulting in the formation of NH_4^+, NO_3^-, SO_4^{2-}, CO_2, and H_2O.

The production of degradation intermediates following SMX decomposition necessitated an evaluation of their environmental impact. To address this concern, the quantitative structure–activity relationship (QSAR) method was employed using the ECOSAR program to predict the toxicity levels of SMX and its degradation by-products on aquatic organism such as fish, daphnids, and green algae(Fig. 8B, C, and Table S7†).[78] The assessment focused on both acute and chronic toxicity levels,
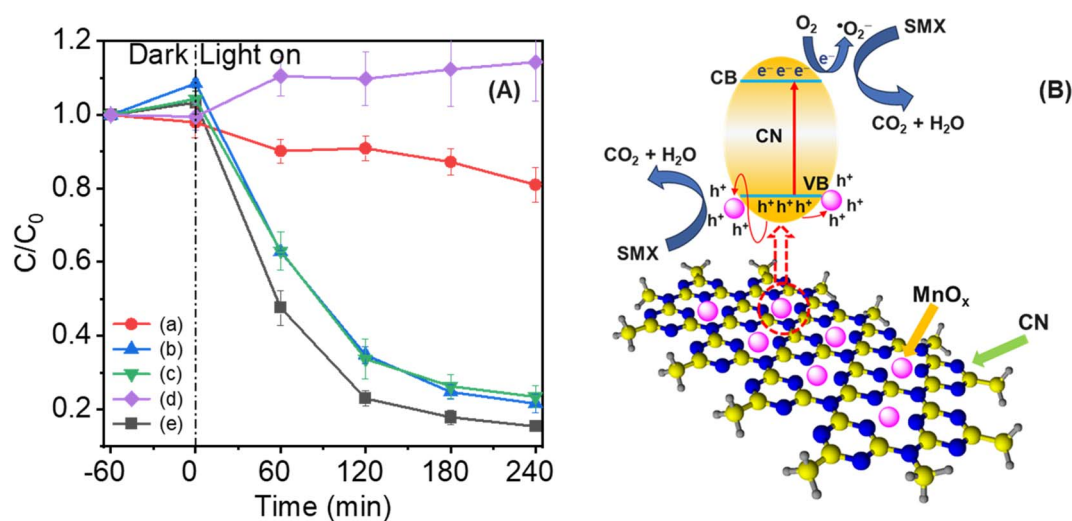

Fig. 7 Scavengers (A) of $K_2Cr_2O_7/e^-$ (a), $Na_2C_2O_4/h^+$ (b), TBA/$\cdot OH$ (c), and BQ/$\cdot O_2^-$ (d), and no scavenger (e); photodegradation mechanism of SMX over 3MnCN under visible light irradiation (B). Conditions: $[SMX]_0 = 15$ mg L^{-1}, $[catalyst]_0 = 200$ mg L^{-1}, $V = 100$ mL, light source: 40 W white LED lamp. The source data is presented in Table S6.†
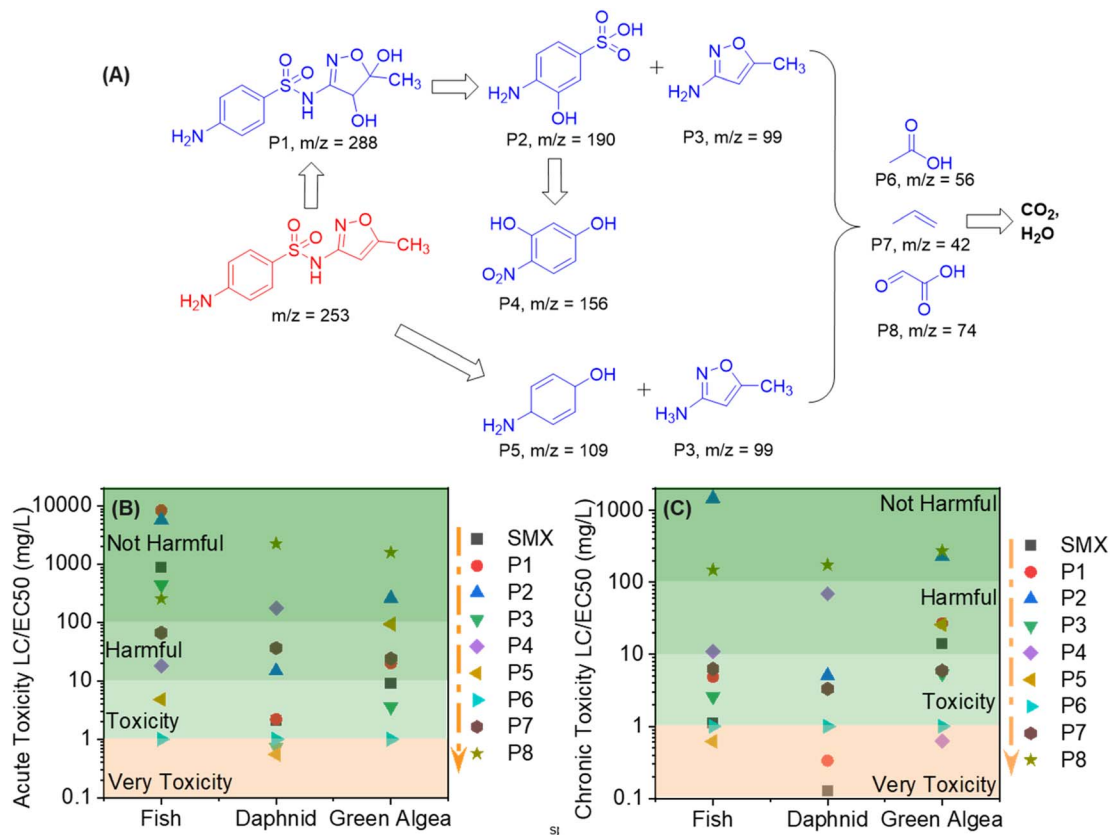
Fig. 8 The proposed SMX photodegradation pathway by 3MnCN (A); change in toxicity during the photodegradation of SMX by 3MnCN *via* ECOSAR (B, C).

revealing that the majority of intermediates displayed significantly higher LC50/EC50/ChV values for these organisms compared to SMX. This QSAR analysis suggests that 3MnCN has the potential to mitigate the toxicity and associated risks posed by SMX.

3.14. Reusability of photocatalyst

The reusability of the 3MnCN material for SMX degradation were evaluated over four consecutive cycles (Fig. 9A). Initially,

the photocatalyst had a degradation efficiency of 85%, which saw a slight reduction to 77% after four cycles. This minor decrease in degradation performance may be attributed to the loss of catalyst during recovery process. Furthermore, XRD patterns (Fig. 9B) of the 3MnCN photocatalyst before and after photocatalytic degradation of SMX showed no noticeable change in peaks after four cycles. TEM image of the reused 3MnCN samples also showed consistent morphology compared to the fresh 3MnCN (Fig. 9C). Besides, the Mn contents of
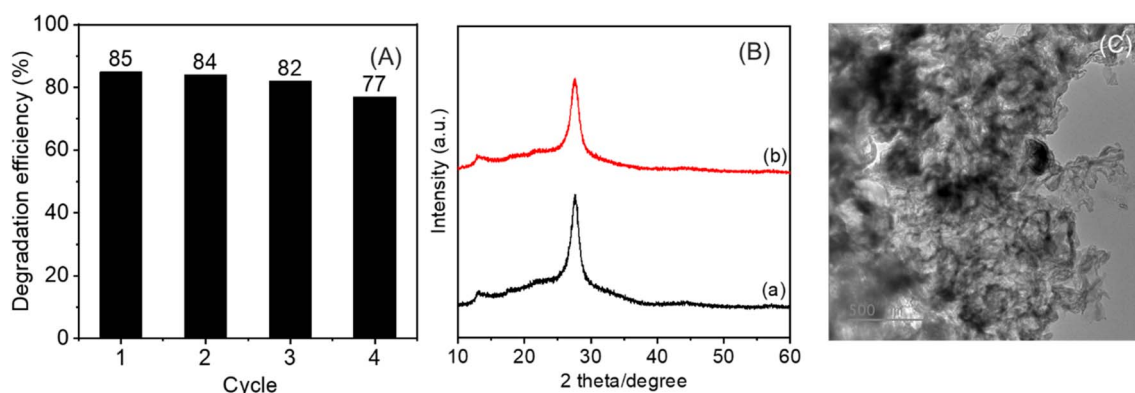

Fig. 9 Recycling of photodegradation (A) of SMX upon the 3MnCN photocatalyst. XRD pattern (B) of 3MnCN of fresh (a) and reuse (b) and TEM image (C) of 3MnCN reuse.

3MnCN sample before and after cycling were analyzed using the ICP-MS method (Fig. S13 and S14†). The result illustrated that the Mn content remained nearly unchanged after recovery compared to the initial value. These findings show that the photocatalytic performance of the 3MnCN material remained stable, demonstrating its effective reusability in the reaction medium. Based on the results of this research, the photocatalyst efficiency of MnO_x/g-C_3N_4 was also compared in terms of photodegradation performance to previous studies (Table S8†).

4. Conclusion

A series of MnO_x/g-C_3N_4 photocatalysts with high photocatalytic activity for SMX degradation have been prepared by facile solvothermal method. The incorporation CN with MnO_x has been effectively improved the photocatalytic performance. Compared with pure CN, 3MnCN enhances separation efficiency of e^- and h^+ when exposed to LED light. The MnO_x/g-C_3N_4 nanocomposite showed outstanding photocatalytic performance with degradation efficiency of SMX (85%), rate constant (3.5×10^{-3} min^{-1}) and high stability toward antibiotic pollutants under visible light irradiation. The SMX degradation pathway was proposed in the MnO_x/g-C_3N_4 nanocomposite to exhibit reduced toxicity toward aquatic organisms. It is anticipated that the innovative MnO_x/g-C_3N_4 catalyst will serve as a practical and efficient catalyst for visible light and a potential material for high-performance photocatalysts for the remediation of pollutants.

Data availability

Data are available on request from the authors.

Conflicts of interest

There are no conflicts to declare.

Acknowledgements

References

1 T. aus der Beek, F. Weber, A. Bergmann, S. Hickmann, I. Ebert, A. Hein and A. Küster, *Environ. Toxicol. Chem.*, 2016, **35**, 823–835.

2 Y. Zhang and S. R. Meshnick, *Antimicrob. Agents Chemother.*, 1991, **35**, 267–271.

3 C. Borsetto, S. Raguideau, E. Travis, D.-W. Kim, D.-H. Lee, A. Bottrill, R. Stark, L. Song, C.-J. Cha, J. Pearson, C. Quince, A. C. Singer and E. M. H. Wellington, *Water Res.*, 2021, **201**, 117382.

4 C. R. dos Santos, Y. A. R. Lebron, V. R. Moreira, K. Koch and M. C. S. Amaral, *Bioresour. Technol.*, 2022, **343**, 126150.

5 T. Thiebault, *Sci. Total Environ.*, 2020, **715**, 136916.

6 S. Rodriguez-Mozaz, S. Chamorro, E. Marti, B. Huerta, M. Gros, A. Sànchez-Melsió, C. M. Borrego, D. Barceló and J. L. Balcázar, *Water Res.*, 2015, **69**, 234–242.

7 Y. Gong, M. Li and Y. Wang, *ChemSusChem*, 2015, **8**, 931–946.

8 X. Wang, S. Blechert and M. Antonietti, *ACS Catal.*, 2012, **2**, 1596–1606.

9 Y. Zheng, J. Liu, J. Liang, M. Jaroniec and S. Z. Qiao, *Energy Environ. Sci.*, 2012, **5**, 6717.

10 S. Cao, J. Low, J. Yu and M. Jaroniec, *Adv. Mater.*, 2015, **27**, 2150–2176.

11 M. Groenewolt and M. Antonietti, *Adv. Mater.*, 2005, **17**, 1789–1792.

12 A. Thomas, A. Fischer, F. Goettmann, M. Antonietti, J.-O. Müller, R. Schlögl and J. M. Carlsson, *J. Mater. Chem.*, 2008, **18**, 4893.

13 Y. Luo, Y. Zhu, Y. Han, H. Ye, R. Liu, Y. Lan, M. Xue, X. Xie, S. Yu, L. Zhang, Z. Yin and B. Gao, *Carbon Res.*, 2023, **2**, 14.

14 A. Hayat, M. Sohail, J. Ali Shah Syed, A. G. Al-Sehemi, M. H. Mohammed, A. A. Al-Ghamdi, T. A. Taha, H. Salem AlSalem, A. M. Alenad, M. A. Amin, A. Palamanit, C. Liu, W. I. Nawawi, M. Tariq Saeed Chani and M. Muzibur Rahman, *Chem. Rec.*, 2022, **22**(7), e202100310.

15 J. Tan, N. Tian, Z. Li, J. Li, X. Yao, M. Vakili, Y. Lu and T. Zhang, *Chem. Eng. J.*, 2021, **421**, 127729.

16 Z. Ding, X. Chen, M. Antonietti and X. Wang, *ChemSusChem*, 2011, **4**, 274–281.

17 S. W. Hu, L. W. Yang, Y. Tian, X. L. Wei, J. W. Ding, J. X. Zhong and P. K. Chu, *Appl. Catal., B*, 2015, **163**, 611–622.

18 S. Cao, J. Low, J. Yu and M. Jaroniec, *Adv. Mater.*, 2015, **27**, 2150–2176.

19 Z. Chen, T.-T. Fan, X. Yu, Q.-L. Wu, Q.-H. Zhu, L.-Z. Zhang, J.-H. Li, W.-P. Fang and X.-D. Yi, *J. Mater. Chem. A*, 2018, **6**, 15310–15319.

20 S. Das, T. Deka, P. Ningthoukhangjam, A. Chowdhury and R. G. Nair, *Appl. Surf. Sci. Adv.*, 2022, **11**, 100273.

21 X. X. Jiang, X. De Hu, M. Tarek, P. Saravanan, R. Alqadhi, S. Y. Chin and M. M. Rahman Khan, *J. CO2 Util.*, 2020, **40**, 101222.

22 H. Cao, Y. Yan, Y. Wang, F.-F. Chen and Y. Yu, *Carbon*, 2023, **201**, 415–424.

23 M. Tanzifi, M. Jahanshahi, M. Peyravi and S. Khalili, *J. Environ. Chem. Eng.*, 2022, **10**, 108600.

24 Y. Li, C. Chen, X. Chen and J. Zang, *Ceram. Int.*, 2021, **47**, 33697–33708.

25 N. Mao, Y. Jiao and X. Duan, *Mater. Res. Bull.*, 2022, **151**, 111818.

26 Y. Meng, W. Song, H. Huang, Z. Ren, S.-Y. Chen and S. L. Suib, *J. Am. Chem. Soc.*, 2014, **136**, 11452–11464.

27 Q. Yuan, D. Liu, N. Zhang, W. Ye, H. Ju, L. Shi, R. Long, J. Zhu and Y. Xiong, *Angew. Chem., Int. Ed.*, 2017, **56**, 4206–4210.

28 W. Gong, Q. Wu, L. Ma, W. Zhang, X. Li, A. Xu and S. Zhao, *Colloids Surf. A Physicochem. Eng. Asp.*, 2023, **659**, 130812.

29 Y. Hong, E. Liu, J. Shi, X. Lin, L. Sheng, M. Zhang, L. Wang and J. Chen, *Int. J. Hydrogen Energy*, 2019, **44**, 7194–7204.

30 X. Zhan, Z. Zhang, J. Lin, J. Xu, X. Wang, B. Hong, Y. Xia and Y. Zeng, *Chem. Eng. J.*, 2024, **489**, 151218.

31 C. Feng, Z. Wang, Y. Ma, Y. Zhang, L. Wang and Y. Bi, *Appl. Catal., B*, 2017, **205**, 19–23.

32 B. Zhu, L. Zhang, B. Cheng and J. Yu, *Appl. Catal., B*, 2018, **224**, 983–999.

33 X. Pan, F. Kong and M. Xing, *Res. Chem. Intermed.*, 2022, **48**, 2837–2855.

34 P. Xia, B. Zhu, B. Cheng, J. Yu and J. Xu, *ACS Sustain. Chem. Eng.*, 2018, **6**, 965–973.

35 C. Fontana, *G. Ital. Chim. Clin.*, 1926, **56**, 396–397.

36 R. Norrestam, N. Ingri, E. Östlund, G. Bloom and G. Hagen, *Acta Chem. Scand.*, 1967, **21**, 2871–2884.

37 L. I. Hill and A. Verbaere, *J. Solid State Chem.*, 2004, **177**, 4706–4723.

38 B. Babu, J. Shim, A. N. Kadam and K. Yoo, *Catal. Commun.*, 2019, **124**, 123–127.

39 J.-X. Sun, Y.-P. Yuan, L.-G. Qiu, X. Jiang, A.-J. Xie, Y.-H. Shen and J.-F. Zhu, *Dalton Trans.*, 2012, **41**, 6756.

40 T. Ma, Q. Shen, J. Xue, B. Zhaoa, R. Guan, X. Liu, H. Jia and B. Xu, *Inorg. Chem. Commun.*, 2019, **107**, 107451.

41 K. S. W. Sing, *Pure Appl. Chem.*, 1985, **57**, 603–619.

42 X. Xu, S. Wang, T. Hu, X. Yu, J. Wang and C. Jia, *Dyes Pigm.*, 2020, **175**, 108107.

43 L. Zhang, M. Zhang, X. Song, H. Wang and Z. Bian, *Chem. Eng. J.*, 2020, **399**, 125825.

44 Y. Liu, Y. Gao, L. Chen, L. Li, D. Ding and Z. Dai, *Sep. Purif. Technol.*, 2023, **307**, 122794.

45 P. V. Zinin, L.-C. Ming, S. K. Sharma, V. N. Khabashesku, X. Liu, S. Hong, S. Endo and T. Acosta, *Chem. Phys. Lett.*, 2009, **472**, 69–73.

46 H. Li, Y. Jing, X. Ma, T. Liu, L. Yang, B. Liu, S. Yin, Y. Wei and Y. Wang, *RSC Adv.*, 2017, **7**, 8688–8693.

47 J. Wang, X. Zuo, W. Cai, J. Sun, X. Ge and H. Zhao, *Dalton Trans.*, 2018, **47**, 15382–15390.

48 Y. Hong, Z. Fang, B. Yin, B. Luo, Y. Zhao, W. Shi and C. Li, *Int. J. Hydrogen Energy*, 2017, **42**, 6738–6745.

49 S. Zhu, X. Cao, X. Cao, Y. Feng, X. Lin, K. Han, X. Li and P. Deng, *Mater. Des.*, 2021, **199**, 109426.

50 J. Singh, A. Arora and S. Basu, *J. Alloys Compd.*, 2019, **808**, 151734.

51 R. Guo, Q. Chen, H. Ding, Q. Wang, W. Pan, N. Yang and C. Lu, *Catal. Commun.*, 2015, **69**, 165–169.

52 Z. Wang, Y. Huo, Y. Fan, R. Wu, H. Wu, F. Wang and X. Xu, *J. Photochem. Photobiol., A*, 2018, **358**, 61–69.

53 Q. Wang, X. Wang, Z. Yu, X. Jiang, J. Chen, L. Tao, M. Wang and Y. Shen, *Nano Energy*, 2019, **60**, 827–835.

54 X. Xu, S. Wang, T. Hu, X. Yu, J. Wang and C. Jia, *Dyes Pigm.*, 2020, **175**, 108107.

55 J.-C. Wang, C.-X. Cui, Q.-Q. Kong, C.-Y. Ren, Z. Li, L. Qu, Y. Zhang and K. Jiang, *ACS Sustain. Chem. Eng.*, 2018, **6**, 8754–8761.

56 J. Miao, J. Sunarso, X. Duan, W. Zhou, S. Wang and Z. Shao, *J. Hazard. Mater.*, 2018, **349**, 177–185.

57 M. Yoshida, T. Yomogida, T. Mineo, K. Nitta, K. Kato, T. Masuda, H. Nitani, H. Abe, S. Takakusagi, T. Uruga, K. Asakura, K. Uosaki and H. Kondoh, *J. Phys. Chem. C*, 2014, **118**, 24302–24309.

58 S. Wang, C. Li, T. Wang, P. Zhang, A. Li and J. Gong, *J. Mater. Chem. A*, 2014, **2**, 2885.

59 Z. Teng, H. Lv, C. Wang, H. Xue, H. Pang and G. Wang, *Carbon*, 2017, **113**, 63–75.

60 M. Wang, M. Shen, L. Zhang, J. Tian, X. Jin, Y. Zhou and J. Shi, *Carbon*, 2017, **120**, 23–31.

61 D. Pan, S. Ge, J. Zhao, Q. Shao, L. Guo, X. Zhang, J. Lin, G. Xu and Z. Guo, *Dalton Trans.*, 2018, **47**, 9765–9778.

62 M. Li, L. Zhang, X. Fan, Y. Zhou, M. Wu and J. Shi, *J. Mater. Chem. A*, 2015, **3**, 5189–5196.

63 H. Zhang, X. Han, H. Yu, Y. Zou and X. Dong, *Sep. Purif. Technol.*, 2019, **226**, 128–137.

64 Y. Liu, Y. Gao, L. Chen, L. Li, D. Ding and Z. Dai, *Sep. Purif. Technol.*, 2023, **307**, 122794.

65 H. N. Tran, S.-J. You, A. Hosseini-Bandegharaei and H.-P. Chao, *Water Res.*, 2017, **120**, 88–116.

66 A. Haara, J. Pykäläinen, A. Tolvanen and M. Kurttila, *J. Environ. Manage.*, 2018, **210**, 71–86.

67 S. Wang and Y. Peng, *Chem. Eng. J.*, 2010, **156**, 11–24.

68 M. A. Qamar, S. Shahid, M. Javed, M. Sher, S. Iqbal, A. Bahadur and D. Li, *Colloids Surf. A Physicochem. Eng. Asp.*, 2021, **611**, 125863.

69 F. Berglund, J. Killander and R. Pompeius, *J. Urol.*, 1975, **114**, 802–808.

70 S. Zhang, H. Gao, J. Li, Y. Huang, A. Alsaedi, T. Hayat, X. Xu and X. Wang, *J. Hazard. Mater.*, 2017, **321**, 92–102.

71 R.-R. Chen, Q.-F. Ren, Y.-X. Liu, Y. Ding, H.-T. Zhu, C.-Y. Xiong, Z. Jin and W.-C. Oh, *J. Korean Ceram. Soc.*, 2021, **58**, 548–558.

72 L. Zhang, M. Zhang, X. Song, H. Wang and Z. Bian, *Chem. Eng. J.*, 2020, **399**, 125825.

73 L. Hu, P. M. Flanders, P. L. Miller and T. J. Strathmann, *Water Res.*, 2007, **41**, 2612–2626.

74 H. Y. Kim, T.-H. Kim, S. M. Cha and S. Yu, *Chem. Eng. J.*, 2017, **313**, 556–566.

75 Y. Li, J. He, K. Zhang, P. Hong, C. Wang, L. Kong and J. Liu, *J. Mater. Sci.*, 2020, **55**, 13767–13784.

76 M. J. García-Galán, M. S. Díaz-Cruz and D. Barceló, *Water Res.*, 2012, **46**, 711–722.

77 A. L. Boreen, W. A. Arnold and K. McNeill, *Environ. Sci. Technol.*, 2005, **39**, 3630–3638.

78 L. Xiang, Z. Xie, H. Guo, J. Song, D. Li, Y. Wang, S. Pan, S. Lin, Z. Li, J. Han and W. Qiao, *Chemosphere*, 2021, **283**, 131156.